International Journal of Applied Power Engineering (IJAPE)
Vol. 15, No. 3, September 2026, pp. 1327~1339
ISSN: 2252-8792, DOI: 10.11591/ijape.v15.i3.pp1327-1339

Modeling and implementation of a dual-mode emulator for line distance protection based on minimum line reactance

Yassine El Asri, Abdellah Lassioui, Hassan El Fadil, Anwar Hasni, Marouane El Ancary, Hafsa Abbade
ISA Laboratory, National School of Applied Sciences (ENSA), Ibn Tofail University, Kénitra, Morocco

Article Info

Article history:

Received Aug 20, 2025
Revised Jun 29, 2026
Accepted Aug 15, 2026

Keywords:

Distance protection
Dual-mode emulator
Overhead transmission lines
Power system protection
Real-time processing

ABSTRACT

Advances in power system protection and the increasing complexity of electrical networks have created a growing need for flexible and cost-effective platforms for testing and validating protection algorithms. However, academic laboratories still face a lack of accessible experimental platforms allowing researchers to implement and evaluate new protection strategies under realistic conditions. This gap is becoming increasingly significant with the emergence of artificial intelligence and data-driven techniques, which require flexible environments for development, testing, and experimental validation. To address this limitation, this work presents the modeling and implementation of a dual-mode emulator for minimum reactance distance protection of overhead transmission lines, operating in both real-time and offline modes. The proposed system acquires and processes voltage and current signals to determine the minimum line reactance used for fault detection and distance estimation. The developed algorithm is evaluated through simulated fault scenarios under different operating conditions. Results demonstrate reliable fault detection and consistent fault-distance estimation. The dual-mode architecture enables both offline analysis of recorded signals and real-time algorithm evaluation. The proposed emulator therefore provides a practical, low-cost academic platform for research, training, and experimental validation of conventional and emerging protection strategies.

Corresponding Author:

Yassine El Asri
ISA Laboratory, National School of Applied Sciences (ENSA), Ibn Tofail University
Kénitra, Morocco
Email: elasriyassine@yahoo.com

1. INTRODUCTION

The protection of high-voltage transmission lines is a fundamental requirement for ensuring the reliability, security, and stability of modern electrical power systems. Among the various protection schemes, distance protection remains one of the most widely adopted solutions for transmission lines, providing both primary and backup protection while offering high selectivity and relatively simple implementation [1]. Nevertheless, the increasing complexity of modern power networks and the emergence of new operating conditions continue to impose significant challenges on conventional distance protection schemes [2].

Distance relays generally determine the location of a fault by evaluating the apparent impedance calculated from voltage and current quantities measured at the relay terminal. The measured impedance is then compared with predefined protection-zone characteristics to determine whether the fault lies within the protected section. Despite the maturity of this principle, the performance of conventional distance protection can be affected by network topology, operating conditions, fault characteristics, and measurement uncertainties [3]. These challenges have motivated the development of improved protection and fault-location techniques capable of maintaining reliable operation under increasingly complex network conditions [4].

One of the major factors affecting impedance-based distance protection is fault resistance. This issue is particularly important for single-line-to-ground faults involving resistive fault paths or arcing phenomena. The additional resistive component can significantly modify the apparent impedance measured by the relay [5]. Consequently, the measured impedance trajectory may be displaced in the R–X plane, potentially resulting in protection-zone underreach, overreach, delayed operation, or even relay maloperation [6]. These effects can reduce the dependability and selectivity of conventional distance protection, especially when accurate and rapid fault clearance is required.

To mitigate the influence of fault resistance, reactance-based fault-location and protection principles provide an attractive alternative to conventional impedance-based approaches. Instead of relying on the magnitude of the complete complex impedance, these methods emphasize its reactive component, which is strongly associated with the electrical distance between the relay location and the fault point. By reducing the contribution of the resistive component to the protection decision, reactance-based approaches can improve fault-distance estimation under resistive fault conditions. However, the measured reactance may still be affected by network configuration, operating conditions, current distribution, and other sources of reactance error; therefore, these effects must be carefully considered when designing the protection algorithm [7].

These considerations are particularly relevant for antenna-configured overhead transmission lines, where radial line sections are supplied predominantly from one end. In such configurations, accurate identification of the faulted section and estimation of the fault location are essential for maintaining protection selectivity and preventing unnecessary disconnection of healthy sections. Recent developments in transmission-line protection further emphasize the need for robust protection algorithms capable of operating reliably under challenging fault and network conditions [8].

In parallel with advances in protection algorithms, real-time simulation and hardware-in-the-loop testing have become increasingly important for the development and validation of power-system protection schemes. These platforms enable protection algorithms and physical relays to be evaluated under controlled and repeatable operating conditions before their deployment in actual power networks [9]. They also provide considerable educational value by allowing students and researchers to reproduce transmission-line faults, configure protection functions, analyze relay responses, and investigate scenarios that would otherwise be difficult, expensive, or unsafe to reproduce on real electrical networks [10].

Accordingly, the objective of this research is to design and implement a dual-mode emulator for minimum-reactance distance protection of antenna-configured overhead transmission lines. The proposed system is capable of operating in both real-time and offline modes, thereby combining experimental validation and post-processing analysis within a single platform. In real-time mode, the emulator acquires and processes electrical quantities to reproduce the behavior of a protection system under actual operating conditions, whereas the offline mode enables previously recorded or simulated fault data to be analyzed without requiring continuous connection to the experimental setup [11], [12]. The proposed platform is therefore intended not only for protection-system development and validation but also as a versatile tool for scientific research and academic training. By integrating fault detection, phase identification, minimum-reactance-based fault localization, and dual-mode operation, the proposed emulator provides a flexible environment for evaluating transmission-line protection algorithms under a wide range of controlled fault scenarios.

2. METHOD

Overhead lines are composed of bare conductors, placed on insulators and fixed to poles (towers) with distances ranging from tens of meters to hundreds of meters. Since these conductors can cause short circuits under the action of wind (conductor oscillations), it is necessary to provide sufficient spacing between the wires. The ground wire is connected to each tower and grounded to dissipate any atmospheric discharges.

The structure, height, and load-bearing capacity of the supports used for overhead lines vary. These include wooden poles, reinforced concrete poles, and concrete towers [13]. Consequently, there are several types of overhead line equipment, which differ according to various standards such as location, spacing, voltage level, and others. Insulators are used to support the conductors and electrically isolate them from the metallic parts of the tower; they can be either suspended or rigidly fixed. Overhead lines (less than 100 kilometers in length) can be represented by the following equivalent diagram [14]. The equivalent circuit used to model an overhead transmission line of less than 100 km is illustrated in Figure 1, showing the main electrical parameters considered in the line representation.

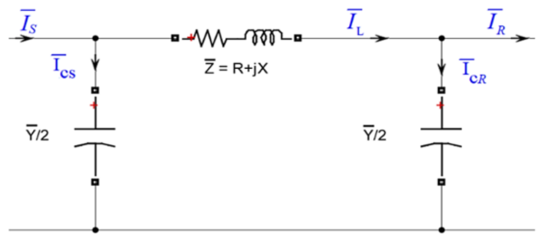

Figure 1. Equivalent diagram of an overhead line

2.1. Overhead transmission line modeling

The diagram consists of the effective longitudinal impedance, composed of the per-unit-length resistance R and the per-unit-length reactance X (1), and the effective transverse impedance, composed of the per-unit-length susceptance (2).

$$Z = R + jX \tag{1}$$

$$Y = jC\omega \tag{2}$$

2.1.1. Measurement of the line characteristics

Line characteristic tests are more effective when performed on a line already installed on towers, in order to take into account the effects of insulators, junctions (jumpers), and environmental conditions. These tests are carried out using primary injection test sets specifically designed for this type of measurement [15]. Figure 2 illustrates the experimental configuration used for the measurement of high-voltage line characteristics, including the connection of the test and measurement equipment at the line terminals.

As reported in Figure 3, the measurement test of the high-voltage transmission line characteristic yielded the essential parameters, including line resistance, reactance, capacitance, and characteristic impedance. These results confirm that direct measurement provides the most reliable approach for obtaining accurate and precise protection settings. This approach ensures proper calibration of protective relays under real operating conditions [16].

2.1.2. Use of predefined average values

Figure 4 illustrates the main characteristics of transmission lines as a function of the conductor material and its cross-sectional area. These characteristics include the cable cross-sectional area, the type of conductor material, the direct resistance per kilometer, the direct reactance per kilometer, the direct impedance per kilometer, the power factor, and the permissible current. The values presented in Figure 4 are therefore used as reference line parameters for the implementation and validation of the proposed minimum reactance-based distance protection method.

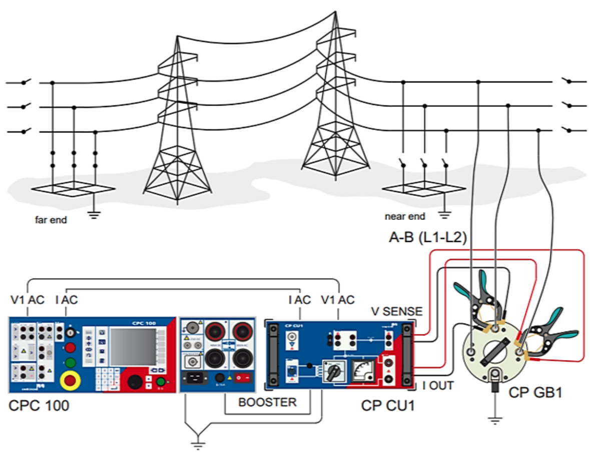

Figure 2. Measured characteristic of high voltage line

Prysmian Group

Cable aislado/*Insulated cable:*
RHAE-RA+2OL 36/66kV 1x1000Al
(26kA,1s)

Código Prysmian/ *Prysmian code:* 20197144

CARACTERÍSTICAS / CHARACTERISTICS

GENERALES/*GENERAL*

Norma constructiva / Norma de referencia *Constructive standard / Standard reference:*	IEC 60840, UNE 211632-1
Tensión, Uo/U(Um) [kV]: *Rated voltage Uo/U(Um)[kV]:*	36/66(72.5)
Tensión a impulsos, Up[kVp]: *Impulse voltage test, Up[kVp]:*	325
Temperatura máxima admisible en el conductor en servicio permanente [ºC]: *Maximum temperature on conductor in normal operation [ºC]:*	90
Temperatura máxima admisible en el conductor en régimen de cortocircuito [ºC]: *Maximum temperature on conductor during short-circuit [ºC]:*	250

DIMENSIONALES /*DIMENSIONAL*

Sección del conductor [mm²]: *Section of conductor* [mm²]:	1000
Peso aproximado [kg/m]: *Approximate weight [kg/m]:*	6.2
Diámetro nominal del conductor [mm]: *Nominal conductor diameter [mm]:*	38.0
Espesor nominal aislamiento [mm]: *Nominal insulation thickness [mm]:*	7.7
Diámetro nominal sobre aislamiento [mm]: *Nominal diameter over insulation [mm]:*	55.9
Sección de la pantalla [mm²]: *Section of screen [mm²]:*	195
Espesor nominal de la cubierta [mm]: *Nominal sheath thickness [mm]:*	3.1
Diámetro nominal exterior [mm]: *Overall nominal diameter [mm]:*	73.0

ELÉCTRICAS /*ELECTRICAL*

Resistencia eléctrica del conductor a 20ºC c.c. [Ω/km]: *Electrical resistance of conductor at 20℃ c.c. [Ω/km]:*	0.0291
Inductancia para cables al tresbolillo y en contacto [mH/km]: *Inductance for cables touching in trefoil [mH/km]:*	0.317
Capacidad nominal [µF/km]: *Nominal capacity [µF/km]:*	0.431
Gradiente eléctrico interno/externo [kV/mm]: *Electrical stress inner/outer [kV/mm]:*	5.6/4.1
Intensidad máxima de cortocircuito en el conductor durante 1.0/1.5 s (90÷250ºC) [kA]: *Conductor short-circuit capacity during 1.0/1.5 s (90÷250ºC) [kA]:*	94.6/77.2
Intensidad máxima de cortocircuito en la pantalla durante 1.0/1.5 s (80÷250ºC) [kA]: *Metallic screen short-circuit capacity during 1.0/1.5 s (80÷250ºC) [kA]:*	26.0/22.4

Revisión/ *Revision:* 2es | 2016-11-10 | Realizado/ *Issued:* J.C.Ruiz | 2/3

Figure 3. Measured characteristic values of a 60 kV line

VALEURS MOYENNES À UTILISER POUR LES LIGNES NON MESURÉES

Sections (mm²)	Rd/km	Xd/km	Zd/km	Cos φ	I admissible (A)
35 Cu	0,50	0,35	0,61	0,819	160
50 Cu	0,42	0,46	0,62	0,677	200
63 Cu	0,3013	0,425	0,521	0,578	226
75 Cu	0,2338	0,4317	0,4908	0,476	265
54 AlAC	0,61	0,43	0,746	0,818	161
116 AlAC	0,2736	0,3503	0,5145 0,4825	0,551	265
147 AlAC	0,2403	0,3583	0,4453	0,516	308
181 AlAC	0,1921	0,3962	0,4404	0,436	353
228 AlAC	0,1678	0,45	0,4793	0,35	415
288 AlAC	0,135	0,434	0,456	0,256	480
366 AlAC	0,128	0,43	0,4491	0,287	560
116 Al.AW	0,2836	0,3503	0,5145 0,4825	0,55	265
147 Al.AW	0,22	0,38	0,45	0,48	308
181,6 AlAW	0,1878	0,3503	0,4332	0,433	353
288 AlAW	0,129	0,428	0,448	0,287	480
366 AlAW	0,098	0,43	0,44	0,223	560
288 Almelec	0,116	0,41			
181,6 Almelec	0,183	0,396	0,4364	0,419	415
228 Almelec	0,146	0,4	0,426	0,343	550
570 Almelec	0,07	0,3559	0,4020	0,174	840
366 Almelec	0,128	0,43	0,4491	0,227	630
148 Almelec	0,225	0,4	0,4589		339

Figure 4. Average values of transmission line characteristics

2.2. Short line model

The capacitance can be neglected without significant error if the lines are less than 100 kilometers in length or if the voltage level does not exceed 66 kV. The short line model per phase is illustrated in Figure 5. It is a simple series circuit. The relationship between the current and the voltage on the line (between the source and the load) can be expressed as (3).

$$\begin{bmatrix} \bar{V}_S \\ \bar{I}_S \end{bmatrix} = \begin{bmatrix} A & B \\ C & D \end{bmatrix} \begin{bmatrix} \bar{V}_R \\ \bar{I}_R \end{bmatrix} \tag{3}$$

In this case, A=D=1 and C=0; therefore, the short transmission line can be represented with these simplified parameters, which indicate that the voltage and current relationships are primarily determined by the series impedance, with no effect from shunt capacitance [17].

$$\begin{bmatrix} \bar{V}_S \\ \bar{I}_S \end{bmatrix} = \begin{bmatrix} 1 & \bar{Z} \\ 0 & 1 \end{bmatrix} \begin{bmatrix} \bar{V}_R \\ \bar{I}_R \end{bmatrix} \tag{4}$$

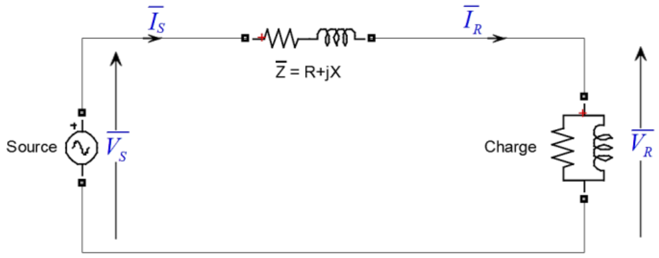

Figure 5. Short line model

2.3. Medium-length lines

For lines with a length between 80 km and 250 km, which are considered medium-length lines, the line charging current becomes significant, and the shunt capacitance must be taken into account. Half of the shunt capacitance can be considered at each end of the line, a configuration known as the nominal π model [18], [19]. The nominal π representation adopted for medium-length transmission lines is presented in Figure 6, where the total shunt capacitance is equally divided between the sending and receiving ends, while the series impedance represents the longitudinal parameters of the line.

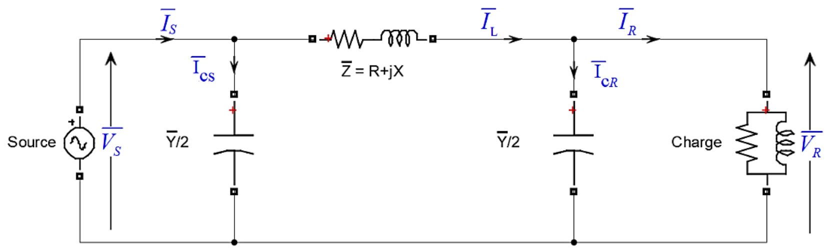

Figure 6. Medium-length line, π representation

The source current and voltage are calculated as follows: from Figure 6, the current in the series impedance, denoted by IL, is given by (5). The source voltage is expressed as (6).

$$\bar{I}_L = \bar{I}_R + \frac{\bar{Y}}{2}\bar{V}_R \tag{5}$$

$$\bar{V}_S = \bar{V}_R + \bar{Z}\bar{I}_L \tag{6}$$

From (5) and (6), we obtain (7) and (8).

$$\bar{V}_S = (1 + \frac{\bar{Y}\bar{Z}}{2})\bar{V}_R + \bar{Z}\bar{I}_R \quad (7)$$

$$\bar{I}_S = (\bar{I}_L + \frac{\bar{Y}}{2})\bar{V}_S \quad (8)$$

$$\bar{I}_S = \bar{Y}(1 + \frac{\bar{Y}\bar{Z}}{4})\bar{V}_R + (1 + \frac{\bar{Y}\bar{Z}}{2})\bar{I}_R \quad (9)$$

Equations (7)-(9) can be written in matrix form as (10).

$$\begin{bmatrix}\bar{V}_S \\ \bar{I}_S\end{bmatrix} = \begin{bmatrix}(1 + \frac{\bar{Y}\bar{Z}}{2}) & \bar{Z} \\ \bar{Y}(1 + \frac{\bar{Y}\bar{Z}}{4}) & (1 + \frac{\bar{Y}\bar{Z}}{2})\end{bmatrix}\begin{bmatrix}\bar{V}_R \\ \bar{I}_R\end{bmatrix} \quad (10)$$

2.4. Long transmission lines

For short and medium lines, the models are obtained by assuming that the line parameters are fixed values. However, if the line length exceeds 250 km, a more accurate solution requires specifying the parameters as being uniformly distributed along the entire length. In this case, the voltage and current vary from one point to another along the line [20]. The distributed-parameter representation of a long transmission line is illustrated in Figure 7, where an elementary section Δx is characterized by its series impedance and shunt admittance, allowing the variations of voltage and current along the line to be considered.

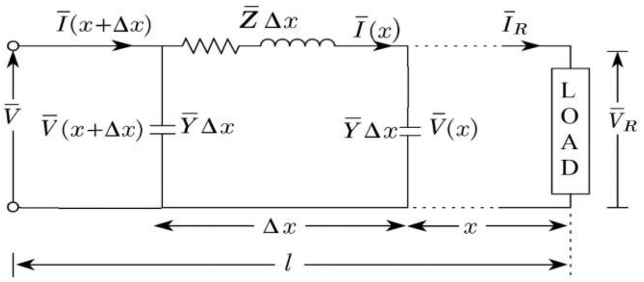

Figure 7. Single-line diagram of a long transmission line

The expressions for the voltage and current at a point x along the line are:

$$\bar{V}(x) = \cosh(\bar{\gamma}x)\bar{V}_R + Z_C\sinh(\bar{\gamma}x)\bar{I}_R \quad (11)$$

$$\bar{I}(x) = \cosh(\bar{\gamma}x)\bar{I}_R + \frac{1}{Z_C}\sinh(\bar{\gamma}x)\bar{V}_R \quad (12)$$

However, when x=lx=l, it is possible to determine the current and voltage magnitudes at the source, with $\bar{V}_S = \bar{V}(l)$ and $\bar{I}_S = \bar{I}(l)$, the result is:

$$\bar{V}(l) = \cosh(\bar{\gamma}l)\bar{V}_R + Z_C\sinh(\bar{\gamma}l)\bar{I}_R \quad (13)$$

$$\bar{I}(l) = \cosh(\bar{\gamma}l)\bar{I}_R + \frac{1}{Z_C}\sinh(\bar{\gamma}l)\bar{V}_R \quad (14)$$

however, the ABCD constants are:

$$\frac{\bar{Y'}}{2} = \frac{1}{Z_C}\tanh(\frac{\bar{\gamma}l}{2}) = \frac{\bar{Y}}{2}\frac{\tanh(\frac{\bar{\gamma}l}{2})}{(\frac{\bar{\gamma}l}{2})} \quad (15)$$

it is now possible to determine a highly accurate equivalent π model for a long transmission line.

$$\bar{V}_S = \left(1 + \frac{\bar{Y}'\bar{Z}'}{2}\right)\bar{V}_R + \bar{Z}'\bar{I}_R \tag{16}$$

$$\bar{I}_S = \left(1 + \frac{\bar{Y}'\bar{Z}}{4}\right)\bar{V}_R + \left(1 + \frac{\bar{Y}'\bar{Z}'}{2}\right)\bar{I}_R \tag{17}$$

Using the expression:

$$\tanh(\frac{\bar{\gamma}l}{2})=\frac{\cosh(\bar{\gamma}l)-1}{\sinh(\bar{\gamma}l)} \tag{18}$$

the parameters of the equivalent π model are obtained as:

$$\bar{Z}' = \overline{Z_C}\sinh(\bar{\gamma}l) = \frac{\overline{Z_C}\sinh(\bar{\gamma}l)}{\bar{\gamma}l} \tag{19}$$

$$\frac{\bar{Y}'}{2} = \frac{1}{\overline{Z_C}}\tanh(\frac{\bar{\gamma}l}{2}) = \frac{\bar{Y}}{2}\frac{\tanh(\frac{\bar{\gamma}l}{2})}{\frac{\bar{\gamma}l}{2}} \tag{20}$$

3. RESULTS AND DISCUSSION

In this section, the proposed embedded solution is presented and evaluated. The system is composed of a central processing unit running LabVIEW software, coupled with dedicated hardware modules to ensure accurate measurement and reliable data acquisition. The hardware architecture integrates a multi-output power supply board, a voltage and current reduction board for signal conditioning, a filtering board to minimize noise, and a National Instruments DAQ6009 card for data acquisition. Together, these components form a complete experimental platform that enables real-time monitoring, fault detection, and validation of the developed algorithms.

Figure 8 illustrates the hardware wiring configuration used for the experimental validation of the proposed solution, showing the interconnection between the Test Universe software, the secondary injection test equipment, and the embedded system. The proposed fault detection and classification algorithm is implemented by processing the measured three-phase voltage and current signals and applying predefined logical conditions to identify the occurrence and type of transmission-line fault. Based on the comparison and combination of these electrical quantities, the corresponding output is activated to indicate the detected fault condition. This implementation represents a key processing stage of the proposed emulator, linking the acquired measurements to the protection decision and enabling the algorithm to be evaluated under different simulated fault scenarios, as illustrated in Figure 9.

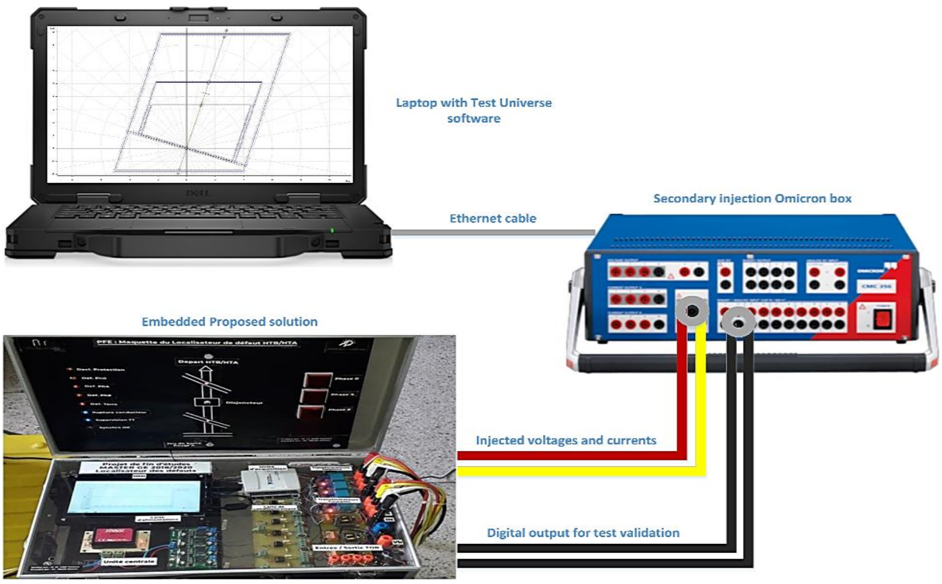

Figure 8. Block diagram of the hardware-in-the-loop test using Omicron CMC356

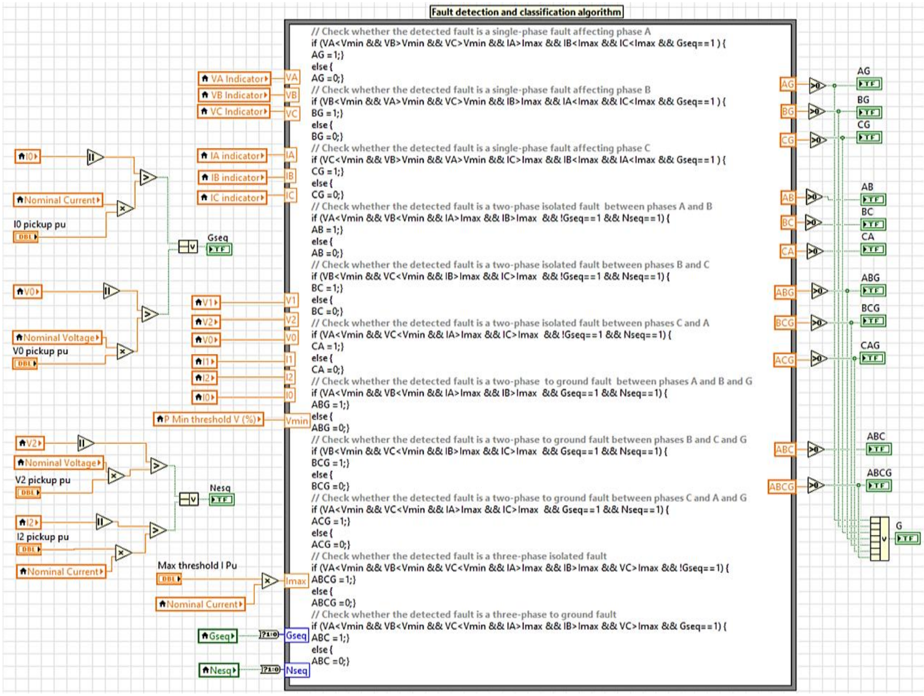

Figure 9. LabVIEW VI for fault detection and classification

By processing the zero, positive, and negative sequence components together with other measured signals, the algorithm accurately determines both the type and location of the fault, providing a high level of reliability in fault detection and classification. In practice, faults on transmission lines rarely exhibit purely resistive behavior, and the variability of resistive elements often reduces the precision of conventional fault location techniques.

The proposed method simplifies the localization task by relying exclusively on line reactance while disregarding the resistive part. This strategy reduces the effect of variable resistance and significantly improves the accuracy and robustness of fault detection.

$$X = \frac{V_\alpha}{I_\alpha + k_0 \cdot 3.I_0} \cdot \sin\left[(\phi V - \phi I).\frac{\pi}{180}\right] \quad (21)$$

$$Fault\ Location = \frac{X}{X_L} \cdot L \quad (22)$$

In (21), the reactance is computed based on the measured quantities of line voltage, line current, zero-sequence current, and the residual compensation factor. The output is expressed in ohms. Equation (22) converts the calculated reactance into a physical fault distance (km) by dividing it by the line reactance per unit length and multiplying by the actual length of the transmission line [21].

After identifying the faulty phase, two algorithms are applied sequentially. The first algorithm confirms the faulted phase and triggers the second algorithm, which selects the appropriate impedance calculation formula according to the detected fault type, as shown in Figure 10. This step extracts the corresponding reactance value, which is then passed to a final algorithm responsible for determining the fault location zone, enabling fault clearance according to the configured protection settings [22], [23].

Once the fault has been detected, confirmed, identified, and classified, the algorithm shown in Figure 11 is triggered to activate the fault zone based on the predefined settings, the real-time measured reactance at the moment of the fault, and the time delay assigned to each zone [24]. The reactance estimation algorithm which dynamically selects the appropriate impedance loop according to the detected fault type (e.g., AG, AB, ABG, three-phase) was experimentally validated on an NI/LabVIEW test bench using secondary injection and COMTRADE replay [25]. The experimental results obtained for different fault types, fault resistances, directions, and injected reactance values are summarized in Table 1.

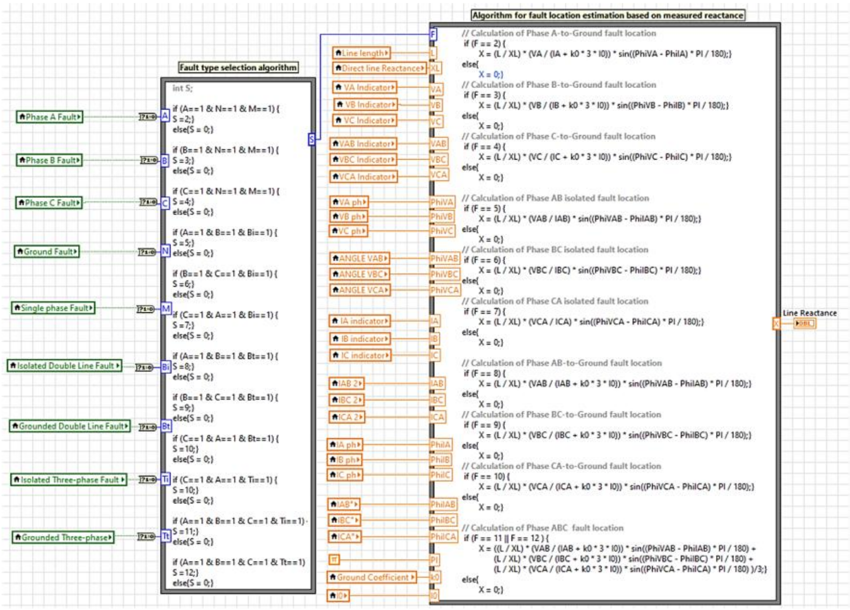

Figure 10. LabVIEW VI for fault reactance calculation

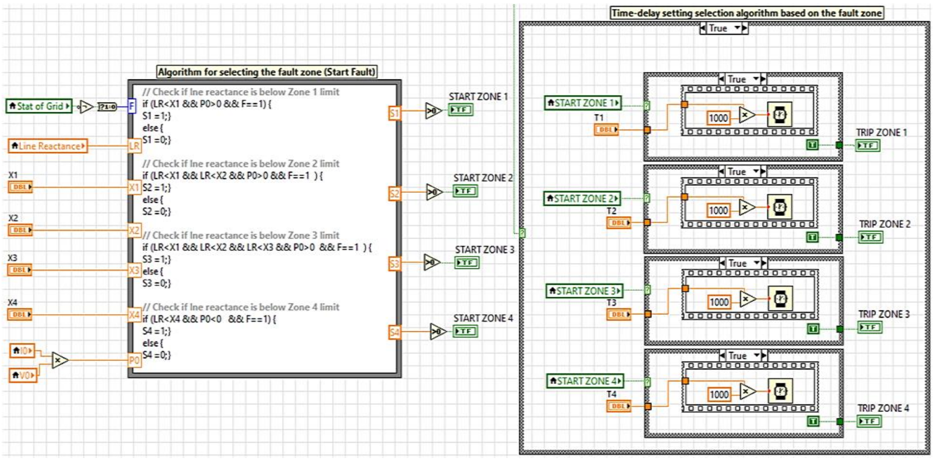

Figure 11. LabVIEW VI for protection zone identification

Table 1. Experimental test results for the algorithms

Fault	Direction	Rf	X injected	X measured	Abs Error	Rel Error %	Result
AG	FWD	0	3.23	3.26	0.03	0.92879	TRUE
AG	FWD	50	3.4	3.46	0.06	1.76471	TRUE
AG	FWD	10	3.57	3.57	0	0	TRUE
BG	FWD	10	3.4	3.43	0.03	0.88235	TRUE
CG	FWD	100	3.23	3.31	0.08	2.47678	TRUE
AB	FWD	0	3.23	3.21	0.02	0.6192	TRUE
ABG	FWD	10	3.4	3.45	0.05	1.47059	TRUE
BC	FWD	50	3.57	3.61	0.04	1.12045	TRUE
BCG	FWD	10	3.57	3.65	0.08	2.2409	TRUE
CA	FWD	0	3.23	3.2	0.03	0.92879	TRUE
CAG	FWD	50	3.4	3.49	0.09	2.64706	TRUE
3PH	FWD	0	3.4	3.38	0.02	0.58824	TRUE
AB	REV	0	1.77	1.79	0.02	1.12994	TRUE

This second validation targets the zone-limit thresholds of the under-reactance distance element. For each protection zone (Z1–Z4), two injections are performed at 95% and 105% of the configured reach Xz. The 95% case must operate (trip) and the 105% case must block (no-trip), provided the directionality (forward for Z1–Z3, reverse for Z4) is satisfied. Results are assessed against a ±5% tolerance around Xz. The results presented in Table 2 confirm the correct behavior of the proposed protection scheme under different test conditions. With a tolerance margin of ±5% around the set impedance values, the system successfully detected and operated within the defined zones for all cases at 95% of the reach, as expected. For the 105% tests, the relay correctly restrained in most cases, confirming that the defined protection-zone boundaries were respected; the misoperation is explained by the fact that the injected fault reactance exceeded the zone threshold by more than 5%, which caused the solution to trigger outside its designated operating region. This behavior is consistent with the expected discrimination margin of the distance protection and highlights that the proposed system maintains its selectivity and reliability within the defined tolerance limits. The theoretical and experimentally measured tripping times obtained for the four protection zones and different fault types are summarized in Table 3.

Table 3 shows that the measured trip times are in close agreement with the theoretical values across all zones and fault types. For Zone 1, instantaneous tripping is observed, with measured delays below 30 ms, reflecting fast relay operation. In Zone 2, the measured times are around 400 ms, with only slight deviations from the theoretical setting. For Zones 3 and 4, the relay trips consistently near 3200 ms, confirming stable time-delayed operation. Overall, the results validate that the protection system performs within the expected tolerances, ensuring both speed and selectivity.

Table 2. Results for different zone faults

Zone	Direction	Percent of reach	X set	X target	Expected operation
Z1	FWD	95	3.397	3.227	Pass
Z1	FWD	105	3.397	3.567	Block / No Trip
Z2	FWD	95	5.095	4.84	Pass
Z2	FWD	105	5.095	5.35	Block / No Trip
Z3	FWD	95	8.838	8.396	Pass
Z3	FWD	105	8.838	9.28	Block / No Trip
Z4	REV	95	1.767	1.679	Pass
Z4	REV	105	1.767	1.855	Block / No Trip

Table 3. Results of time tripping for different zone faults

Zone	Direction	Fault	Theoretical trip time (ms)	Measured trip time (ms)
Z1	FWD	AG	0	22
Z1	FWD	AB	0	20
Z1	FWD	ABG	0	26
Z1	FWD	3PH	0	17
Z2	FWD	AG	400	398
Z2	FWD	AB	400	429
Z2	FWD	ABG	400	435
Z2	FWD	3PH	400	415
Z3	FWD	AG	3200	3215
Z3	FWD	AB	3200	3242
Z3	FWD	ABG	3200	3247
Z3	FWD	3PH	3200	3209
Z4	REV	AG	3200	3241
Z4	REV	AB	3200	3210
Z4	REV	ABG	3200	3241
Z4	REV	3PH	3200	3214

4. CONCLUSION

The proposed emulator demonstrates reliable performance, as the experimental results show good agreement with the theoretical calculations under the different tested operating conditions. By directly exploiting measured impedance values, the proposed solution achieves more precise fault identification and decision-making, showing robustness even under varying fault resistances that typically challenge traditional schemes. This capability significantly enhances the selectivity, dependability, and security of fault clearance, ensuring that protective relays operate only within their intended zones. Moreover, the embedded design offers flexibility and adaptability, making it suitable for both laboratory studies and real-world deployment in modern power grids. Looking ahead, future developments will focus on integrating advanced approaches such as traveling-wave–based fault location, optimization through genetic algorithms, and intelligent classification using artificial neural networks. The incorporation of artificial intelligence techniques is expected to further improve adaptability and self-learning capabilities, ultimately leading to next-generation protection systems that combine speed, accuracy, and resilience against evolving grid conditions.

FUNDING INFORMATION

Authors state no funding involved.

AUTHOR CONTRIBUTIONS STATEMENT

This journal uses the Contributor Roles Taxonomy (CRediT) to recognize individual author contributions, reduce authorship disputes, and facilitate collaboration.

Name of Author	C	M	So	Va	Fo	I	R	D	O	E	Vi	Su	P	Fu
Yassine El Asri	✓	✓	✓	✓	✓	✓	✓	✓	✓	✓	✓		✓	✓
Abdellah Lassioui	✓	✓		✓		✓	✓			✓	✓	✓		
Hassan El Fadil	✓	✓		✓	✓	✓			✓			✓		
Anwar Hasni		✓		✓		✓				✓				
Marouane El Ancary	✓			✓	✓	✓				✓			✓	
Hafsa Abbade		✓	✓		✓		✓			✓	✓			

C : **C**onceptualization
M : **M**ethodology
So : **So**ftware
Va : **Va**lidation
Fo : **Fo**rmal analysis
I : **I**nvestigation
R : **R**esources
D : **D**ata Curation
O : Writing - **O**riginal Draft
E : Writing - Review & **E**diting
Vi : **Vi**sualization
Su : **Su**pervision
P : **P**roject administration
Fu : **Fu**nding acquisition

CONFLICT OF INTEREST STATEMENT

Authors state no conflict of interest.

DATA AVAILABILITY

The data supporting the findings of this study are available from the corresponding author, upon reasonable request.

REFERENCES

[1] R. Pujari and M. N. Alam, "Distance relaying for the protection of modern power system networks," *IEEE Access*, vol. 13, pp. 28861–28893, 2025, doi: 10.1109/ACCESS.2025.3539919.

[2] Y. Li, H. Wu, and X. Wang, "Challenges for distance relays in grid code-compliant inverter-based power systems: a review," *IEEE Open Journal of Power Electronics*, vol. 7, pp. 128–145, 2026, doi: 10.1109/OJPEL.2025.3640291.

[3] A. W. D. Sarmiento, J. S. L. Colqui, and J. P. Filho, "Overhead transmission line modeling strategies for EMT-based traveling-wave analysis and fault location," *IEEE Access*, vol. 13, pp. 140462–140472, 2025, doi: 10.1109/ACCESS.2025.3597218.

[4] P. Khameneh, H. Daryabar, M. Abedini, and M. Davarpanah, "A fault-location-based accelerated trip scheme for distance protection in IBR-integrated networks," *IEEE Access*, vol. 13, pp. 181313–181322, 2025, doi: 10.1109/ACCESS.2025.3623510.

[5] M. S. Shaikh, S. Raj, S. A. Latif, W. F. Mbasso, and S. Kamel, "Optimizing transmission line parameter estimation with hybrid evolutionary techniques," *IET Generation, Transmission & Distribution*, vol. 18, no. 9, pp. 1795–1814, May 2024, doi: 10.1049/gtd2.13157.

[6] A. Khoshkalam and D. Ali, "The impacts of the transmission line length in an interconnected micro-grid on its performance and protection at different fault levels," *Green Technology, Resilience, and Sustainability*, vol. 4, no. 1, p. 1, Feb. 2024, doi: 10.1007/s44173-024-00016-y.

[7] M. S. Shaikh, H. Lin, G. Zheng, C. Wang, Y. Lin, and X. Dong, "Innovative hybrid grey wolf-particle swarm optimization for calculating transmission line parameter," *Heliyon*, vol. 10, no. 19, p. e38555, Oct. 2024, doi: 10.1016/j.heliyon.2024.e38555.

[8] R. Mugabe, M. R. Atim, J. Obungoloch, and J. N. Wanzala, "Dynamic transmission line modeling and real-time fault analysis using ABCD parameters enhanced by equivalent π -model for accurate efficiency and voltage stability assessment," *Engineering Research Express*, vol. 7, no. 4, p. 0453b4, Dec. 2025, doi: 10.1088/2631-8695/ae2bbe.

[9] M. Yang *et al.*, "A time-domain fault location technique for HVDC transmission lines based on numerical solution of differential equation," *International Journal of Electrical Power & Energy Systems*, vol. 170, p. 110867, Sep. 2025, doi: 10.1016/j.ijepes.2025.110867.

[10] N. Alam, M. A. Rahman, and M. R. Islam, "DynaLiRD: a dataset for dynamic line rating of overhead transmission lines, utilizing meteorological data and grid parameters based on the IEEE 738–2012 standard," *Data in Brief*, vol. 62, p. 112065, Oct. 2025, doi: 10.1016/j.dib.2025.112065.

[11] Y. El Asri *et al.*, "PV emulator based on DC-DC buck converter and PI controller," *EPJ Web of Conferences*, vol. 330, p. 01002, Jun. 2025, doi: 10.1051/epjconf/202533001002.

[12] Y. El Asri *et al.*, "Enhanced PV emulator performance using DC-DC buck converter," in *Lecture Notes in Networks and Systems*, vol. 1641 LNNS, 2026, pp. 415–425, doi: 10.1007/978-3-032-06061-7_33.

[13] D. C. Huynh and L. D. Ho, "Comprehensive fault location on transmission lines considering variation in line parameters and saturation in current transformers," *IEEE Access*, vol. 13, pp. 734–769, 2025, doi: 10.1109/ACCESS.2024.3522252.

[14] K. Osmani and D. Schulz, "A drone-deployable remote current sensor for non-invasive overhead transmission lines monitoring," *IEEE Access*, vol. 13, pp. 62393–62411, 2025, doi: 10.1109/ACCESS.2025.3554570.

[15] P. Gomez, "Electromagnetic transient model reconstruction of generalized power transmission lines based on time-synchronized waveform measurements," *IEEE Access*, vol. 13, pp. 173895–173908, 2025, doi: 10.1109/ACCESS.2025.3617222.
[16] H. Alafnan, M. Alangari, D.-E. A. Mansour, and X. Pei, "Enhancing instantaneous overcurrent protection selectivity in power lines using resistive superconducting fault current limiters," *IEEE Access*, vol. 13, pp. 202643–202654, 2025, doi: 10.1109/ACCESS.2025.3638142.
[17] F. P. de Albuquerque, R. F. R. Pereira, E. C. M. da Costa, and L. H. B. Liboni, "Nonlinear solutions applied to parameter estimation of overhead transmission lines and submarine cables in offshore facilities," *IET Generation, Transmission & Distribution*, vol. 17, no. 23, pp. 5286–5297, Dec. 2023, doi: 10.1049/gtd2.13039.
[18] Z. M. Ali and E. M. Esmail, "Deep learning and wavelet packet transform for fault diagnosis in double circuit transmission lines," *Scientific Reports*, vol. 15, no. 1, p. 30145, Aug. 2025, doi: 10.1038/s41598-025-15583-8.
[19] S. Cao, J. Xu, H. Wang, M. Feng, and G. Li, "A real-time simulation model of transmission lines incorporating specific frequency dependence," *IEEE Transactions on Industrial Informatics*, vol. 21, no. 7, pp. 5504–5513, Jul. 2025, doi: 10.1109/TII.2025.3556027.
[20] H. Chen, Z. Hu, Z. Wang, J. Tan, X. Xu, and Z. Sun, "New method for live line measuring the zero-sequence distribution parameters for partial parallel double-circuit transmission lines," *International Journal of Electrical Power & Energy Systems*, vol. 169, p. 110763, Aug. 2025, doi: 10.1016/j.ijepes.2025.110763.
[21] Y. El Asri, H. El Fadil, A. Lassioui, A. Jbari, A. Hasni, and M. El Ancary, "Real time fault detection, classification and localization in transmission lines with LabVIEW acquisition and processing," *International Review of Electrical Engineering (IREE)*, vol. 20, no. 2, p. 100, Apr. 2025, doi: 10.15866/iree.v20i2.25910.
[22] T. Hagan, D. Senaratne, R. Meier, E. Cotilla-Sanchez, and J. Kim, "Implementing power system protection algorithms in a digital hardware-in-the-loop substation," *IEEE Open Access Journal of Power and Energy*, vol. 10, pp. 270–282, 2023, doi: 10.1109/OAJPE.2022.3229413.
[23] T. Penthong, M. Ginocchi, A. Ahmadifar, F. Ponci, and A. Monti, "IEC 61850-based protection scheme for multiple feeder faults and hardware-in-the-loop platform for interoperability testing," *IEEE Access*, vol. 11, pp. 65181–65196, 2023, doi: 10.1109/ACCESS.2023.3280128.
[24] N. George, O. D. Naidu, and A. Kumar Pradhan, "Source-agnostic single-ended protection and fault location for double-circuit lines connected to power electronics-based sources," *IEEE Access*, vol. 13, pp. 132038–132051, 2025, doi: 10.1109/ACCESS.2025.3590962.
[25] J. R. Camarillo-Penaranda, M. Aredes, and G. Ramos, "Hardware-in-the-loop testing of a distance protection relay," *IEEE Transactions on Industry Applications*, vol. 57, no. 3, pp. 2326–2331, May 2021, doi: 10.1109/TIA.2021.3066328.

BIOGRAPHIES OF AUTHORS

Yassine El Asri received the Master of Research degree in electrical engineering from ENSET Rabat, Morocco, in 2020. He is currently pursuing the Ph.D. degree in the Advanced Systems Engineering Laboratory at ENSA Kenitra, Morocco. He has more than eight years of professional experience in the commissioning of high-voltage network protection systems at ONEE, and four years of teaching experience as a professional instructor in electronics and automation. His main research interests include renewable energy emulators and storage systems. He can be contacted at email: elasriyassine@yahoo.com.

Abdellah Lassioui received his Diploma of State Engineer in Electrical Engineering from the University of Sciences and Techniques, Tangier, Morocco, in 2015. He received his Ph.D. in automatic control in 2021, Université Ibn Tofail, Kénitra, Morocco. He is currently with the ISA Laboratory. Since 2022, he has been successively an assistant professor at the Ecole Nationale des Sciences Appliquées, Université Ibn Tofail, Kénitra, Morocco. His current research interests include the fields of nonlinear control of power electronic systems, electric vehicles, and wireless power transfer charging for electric vehicles. He has co-authored over 40 journal and conference papers. He can be contacted at email: abdellah.lassioui@uit.ac.ma.

Hassan El Fadil received his B.S. degree in electronics, the Agrégation degree in electrical engineering, the M.S. degree in automatic control, and the Ph.D. degree in automatic control from the Ecole Mohammadia d'Ingénieurs, Université Mohammed V, Rabat, Morocco, in 1994, 1999, 2003, and 2008, respectively. He is currently with the ISA Laboratory. His research interests include nonlinear and adaptive control, power converters and electric motors control, renewable energy, distributed energy resources, smart grid, and electric vehicles. He has published over 160 journal/conference papers. He can be contacted at email: elfadilhassan@yahoo.fr.

Anwar Hasni received his State Engineer Diploma in electrical engineering from the National School of Applied Sciences (ENSA), Ibn Tofail University, Kenitra, Morocco, in 2023. He is currently pursuing a Ph.D. in electrical engineering at the ISA Laboratory of ENSA, Ibn Tofail University. His research interests focus on nonlinear control of power electronic systems, electric vehicles, and adaptive cruise control for electric vehicles. He can be contacted at email: hasni.anwar20@gmail.com.

Marouane El Ancary received his Agrégation degree in electrical engineering from the Ecole Normale Supérieure de l'Enseignement Technique (ENSET) at Mohammed V University in Rabat, Morocco, in 2012. He also earned an M.S. degree in electronic engineering from Abdelmalek Essaadi University in Tetouan, Morocco, in 2021. He is currently pursuing a Ph.D. in electrical engineering at the ISA Laboratory at the National School of Applied Sciences (ENSA), Ibn Tofail University, Kenitra, Morocco. His primary research areas include electric vehicles, wireless power transfer chargers, control systems, and optimization. He can be contacted at email: marouane.elancary@gmail.com.

Hafsa Abbade is an electrical and renewable energy engineer from the National School of Applied Sciences (ENSA), Ibn Tofail University, Kenitra, Morocco, in 2024. Currently, she is pursuing a Ph.D. in electrical engineering at the ISA Laboratory of ENSA. Her research is centered on the intelligent control and energy management system for hydrogen electric vehicles. She is passionate about green hydrogen and fuel cell electric vehicles (FCEVs). She can be contacted at email: hafsa.abbade@uit.ac.ma.